

# Electrical Characterization of Thermally Activated Defects in $n$ -Type Float-Zone Silicon

Yan Zhu , Fiacre Rougieux , Nicholas E. Grant , Joyce Ann T. De Guzman , John D. Murphy ,  
Vladimir P. Markevich , Gianluca Coletti , Anthony R. Peaker , and Ziv Hameiri

## I. INTRODUCTION

**Abstract**—Float-zone (FZ) silicon is usually assumed to be bulk defect-lean and stable. However, recent studies have revealed that detrimental defects can be thermally activated in FZ silicon wafers and lead to a reduction of carrier lifetime by up to two orders of magnitude. A robust methodology which combines different characterization techniques and passivation schemes is used to provide new insight into the origin of degradation of 1  $\Omega$ -cm  $n$ -type phosphorus doped FZ silicon (with nitrogen doping during growth) after annealing at 500 °C. Carrier lifetime and photoluminescence experiments are first performed with temporary room temperature surface passivation which minimizes lifetime changes which can occur during passivation processes involving thermal treatments. Temperature- and injection-dependent lifetime spectroscopy is then performed with a more stable passivation scheme, with the same samples finally being studied by deep level transient spectroscopy (DLTS). Although five defect levels are found with DLTS, detailed analysis of injection-dependent lifetime data reveals that the most detrimental defect levels could arise from just two independent single-level defects or from one two-level defect. The defect parameters for these two possible scenarios are extracted and discussed.

**Index Terms**—Defects, deep level transient spectroscopy (DLTS), float-zone (FZ), lifetime, recombination, silicon.

Manuscript received September 10, 2020; revised October 9, 2020; accepted October 9, 2020. Date of publication October 29, 2020; date of current version December 21, 2020. This work was supported in part by the Australian Government through Australian Centre for Advanced Photovoltaics under Grant RG200768-G, and in part by the Australian Renewable Energy Agency under Grant 2017/RND001. The work of Nicholas E. Grant was supported in part by the EPSRC under Grant EP/M024911/1 and Grant EP/J01768X/2, and in part by the International and Industrial Engagement Fund of the EPSRC SUPERSOLAR Solar Energy Hub under Grant EP/J017361/1. The work of Vladimir P. Markevich and Anthony R. Peaker was supported by the U.K. EPSRC under Grant EP/T025131/1 and Grant EP/M024911/1. The work of Joyce Ann T. De Guzman was supported by the Government of the Philippines for funding the Ph.D. course through the Department of Science and Technology. (Corresponding author: Yan Zhu.)

Yan Zhu, Fiacre Rougieux, and Ziv Hameiri are with the University of New South Wales, Sydney, NSW 2052, Australia. (e-mail: yan.zhu@unsw.edu.au; fiacre.rougieux@unsw.edu.au; z.hameiri@unsw.edu.au).

Nicholas E. Grant and John D. Murphy are with the University of Warwick, CV4 7AL Coventry, U.K. (e-mail: nicholas.e.grant@warwick.ac.uk; john.d.murphy@warwick.ac.uk).

Joyce Ann T. De Guzman, Vladimir P. Markevich, and Anthony R. Peaker are with The University of Manchester, M13 9PL Manchester, U.K. (e-mail: joyceann.deguzman@postgrad.manchester.ac.uk; v.markevich@manchester.ac.uk; a.peakier@manchester.ac.uk).

Gianluca Coletti is with the University of New South Wales, Sydney, NSW 2052, Australia, and also with TNO Energy Transition, Solar Energy, 1755 LE Petten, The Netherlands (e-mail: gianluca.coletti@tno.nl).

Color versions of one or more of the figures in this article are available online at <https://ieeexplore.ieee.org>.

Digital Object Identifier 10.1109/JPHOTOV.2020.3031382

Float-ZONE (FZ) silicon is considered to have high purity and little contamination [1]. For photovoltaic applications, FZ silicon wafers are often used for high efficiency solar cells [2]–[4]. FZ silicon is often assumed to be stable and bulk defect-free, thus it has been used as control materials in many studies of defects or degradation phenomena in silicon grown by other techniques [5]–[7]. FZ silicon wafers are also frequently used for the studies of silicon surface passivation quality [8]–[10], and for the parameterization of intrinsic recombination in silicon [11].

However, recent research has found that boron-doped  $p$ -type FZ silicon can suffer from light-induced degradation at elevated temperature (around 75 °C) [12], [13]. The degradation is found to be similar to the ones observed in multicrystalline silicon [14], [15].

Apart from this light-induced degradation, it has been revealed that bulk defects with strong recombination activity can be formed in FZ silicon upon thermal processing. These defects are found to be activated by heat treatments in the temperature range from 450 °C to 700 °C [16]. Unlike the light-induced degradation in FZ silicon which was mainly identified in  $p$ -type material (except that a recent study observed a weak degradation in 200  $\Omega$ -cm  $n$ -type FZ silicon [17]), these thermally activated defects can have a substantial impact in both  $n$ -type and  $p$ -type FZ silicon [16], [18]. After formation, these defects can be permanently annihilated by an annealing at temperature above 1000 °C for 30 min. Further annealing at lower temperatures does not result in reactivation of the defects [18]. A recent study showed that the defect activation takes places on subsecond time scale and illumination with photon energy above the bandgap can decrease the onset temperature of degradation [19]. The defect deactivation is also found to occur within a short period of time (1 min at 1000 °C). However, a prolonged high temperature annealing is required for a complete and irreversible defect annihilation [19].

These thermally activated defects are very detrimental. A full activation can reduce the lifetime of minority carriers in silicon wafer from above a millisecond to about 10  $\mu$ s [16], [18]. It should be noted that the deposition temperatures of several common dielectrics, such as silicon nitride ( $\text{SiN}_x$ ) via plasma-enhanced chemical vapor deposition (PECVD), can be in the temperature range where the recombination active defects are formed. Activation anneals for aluminum oxide surface passivation are also often performed in this temperature range [20].

Previous studies found that these thermally activated defects can be partially passivated via hydrogenation [19], [21], [22]. Therefore, these defects could be activated during the surface passivation process, but also be partially passivated by the hydrogen introduced during the dielectric deposition process. It was also shown that the partial passivation provided by hydrogen is only temporary [19]. The assumption that FZ silicon is bulk defect-free is therefore not always a correct one.

The origin of these thermally activated defects is not fully understood yet. Several studies have indicated that they are related to vacancies formed in the wafers during the FZ silicon growth [16], [18], [21], [23]. From photoluminescence (PL) images of the degraded FZ silicon wafers, it has been found that the activated defects have a much higher concentration in the center circular area than in the periphery of the wafers [16]. This correlates with the distribution of vacancy-related defects in FZ silicon grown with a relatively high growth speed [24]–[27]. Moreover, a few studies have also indicated that nitrogen doping during the FZ silicon growth plays a significant role in the formation of recombination active defects [18], [21], [23]. Via secondary ion mass spectrometry, a recent study showed that the permanent defect annihilation requires effusion of nitrogen impurities from the wafer, indicating the involvement of nitrogen in the defect formation [19].

The detailed electrical properties of the defects have been mainly investigated by deep level transient spectroscopy (DLTS) and minority carrier transient spectroscopy (MCTS) [16], [18], [19], [23]. Several defect levels have been assigned to the thermally activated defects. However, the relative recombination activities of these levels have not been fully determined. Therefore, it is not clear which (if any) of these defect levels are responsible for the severe reduction of carrier lifetime.

Lifetime spectroscopy is a defect characterization technique sensitive to recombination active defects [28]. Thus, it is suitable for characterizing the most detrimental defect levels. Injection-dependent lifetime spectroscopy (IDLS) has previously been applied to study thermally activated defects in FZ silicon [21]. However, due to the fundamental ambiguity of IDLS, the defect parameters were not extracted, and only a constraint of the defect parameters was given. By measuring injection-dependent lifetime at various temperatures (TIDLS) [29] or at various doping concentrations ( $N_{\text{dop}}$ -IDLS) [28], [30], it is possible to reduce the ambiguity of defect parameterization in IDLS [28], [31].

In this article, we combine TIDLS with DLTS/MCTS to characterize the most detrimental defect levels among the thermally activated defects in *n*-type FZ silicon. We also provide a thorough analysis of their electrical properties.

## II. EXPERIMENTAL METHODS

In this article, a set of phosphorus doped *n*-type FZ silicon wafers grown in a nitrogen ambient from the same manufacturer was used. The wafers were circular with a diameter of 100 mm, 190  $\mu\text{m}$  thick, and have a resistivity of 1  $\Omega\cdot\text{cm}$ . The wafers were divided into three groups (labeled as Groups A, B, and C). Each group contains three to four wafers to improve the

statistics of the measurements. Wafers in Group A were not annealed. Wafers in Group B were annealed at 500  $^{\circ}\text{C}$  in a nitrogen ambient for 30 min. According to previous studies [16], [18], [19], this annealing should activate the defects and lead to a significant lifetime reduction in the wafers. Wafers in Group C were annealed at 1000  $^{\circ}\text{C}$  in a nitrogen ambient for 30 min. The annealing was completed in a tube furnace with no above-bandgap light incident on the samples other than that from the furnace element (which is negligible at 500  $^{\circ}\text{C}$ ). According to previous studies, this annealing should stabilize the lifetime in the FZ silicon and prevent any further degradation due to the thermally activated defects [16], [18], [19].

For the first characterization stage, after the corresponding annealing process, all the wafers went through a superacid-derived passivation process based on bis(trifluoromethane)sulfonimide (TFSI) in 1, 2-dichloroethane [32], [33]. This passivation scheme has been shown to provide an excellent passivation quality with a surface recombination velocity (SRV) around 1 cm/s for wafers with similar resistivity [32]. It is also stable for enough time to undertake room temperature PL imaging and injection-dependent lifetime measurements. Moreover, it is a process conducted at room temperature, thus, no thermal budget or bulk hydrogen is added to the wafers, which is very important for the investigation of defects that are sensitive to processing at elevated temperatures. PL imaging was performed with a BT Imaging LIS-L1 system and lifetime measurements were made with a Sinton WCT-120 lifetime tester.

The superacid-derived passivation is not stable enough for TIDLS measurements, so at the second characterization stage, all wafers were repassivated by amorphous silicon (a-Si) via PECVD. The wafers were Radio Corporation of America cleaned before the deposition. The deposition temperatures were kept below 200  $^{\circ}\text{C}$  to minimize the thermal budget on the samples and the potential hydrogen induced passivation of the defects. The passivation quality and stability of the a-Si passivation scheme were tested with a separate set of FZ wafers. It was found that the a-Si passivation can achieve an SRV below 10 cm/s and remain stable up to 200  $^{\circ}\text{C}$ . After the a-Si passivation, TIDLS measurements of the wafers were performed at temperatures in the range from  $-50$   $^{\circ}\text{C}$  to 150  $^{\circ}\text{C}$  with a customized temperature dependent carrier lifetime tester [34]. Due to the nonuniform distribution of the defects, the lifetime of the degraded wafers (Group B) were measured in the center area (using a circular sensor area with diameter of 28 mm) where the defects have a relatively high concentration and uniform distribution. After the lifetime measurements at elevated temperatures, the carrier lifetime of the samples was remeasured at room temperature to check if the sample lifetime had changed during the TIDLS measurements.

For the third characterization stage which utilized DLTS and MCTS measurements, the a-Si layers were stripped off from the samples with a mixture of 49% hydrofluoric acid (HF) and 69% nitric acid (ratio of 1:10) for 2 min, followed by rinsing in deionized water. Schottky barrier diodes (SBDs) and ohmic contacts were fabricated by thermal evaporation of metal layers onto the sample surfaces subjected to cleaning and dipping in diluted HF prior to the evaporation. For the SBDs, gold was

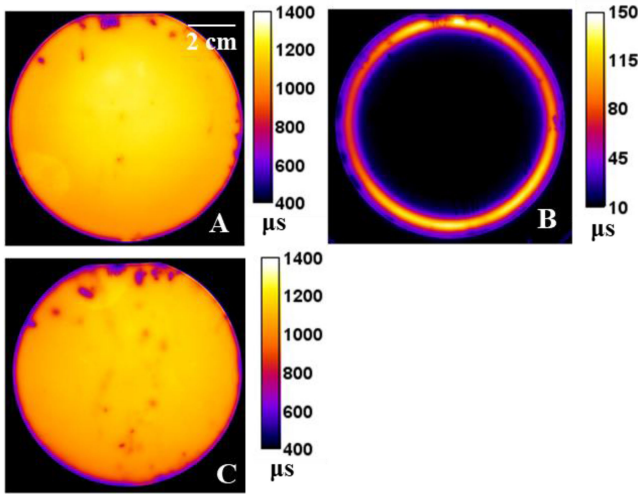


Fig. 1. Calibrated PL images for one 100 mm diameter wafer from each group with room temperature superacid-derived surface passivation. The wafer from Group A was not annealed, the wafer from Group B was annealed at 500 °C for 30 min, and the wafer from Group C was annealed at 1000 °C for 30 min.

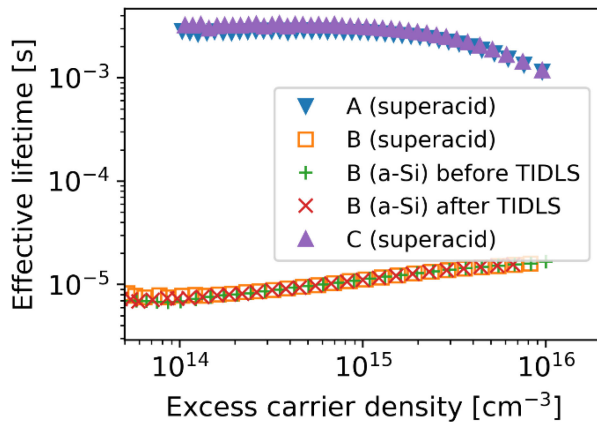


Fig. 2. Room temperature effective lifetime curves for a representative sample from each group after superacid-derived surface passivation. The lifetimes of the sample from Group B (500 °C anneal) with a-Si surface passivation before and after TIDLs measurements are also shown.

evaporated through a shadow mask. For the ohmic contact, an aluminum layer was evaporated at the back surface. For MCTS measurements, an open area at the back side of the samples was left for the optical excitation using a 940 nm light emitting diode. All these processes were undertaken close to room temperature.

### III. RESULTS AND DISCUSSIONS

#### A. Thermal Activation of the Defects

Room temperature lifetime and PL imaging measurements were performed on all wafers with superacid-derived surface passivation. The calibrated PL images (under one sun illumination) of one typical wafer from each group are shown in Fig. 1. The measured injection dependent lifetime curves are shown in Fig. 2.

As can be seen, the wafer from Group B (annealed at 500 °C) shows a much lower lifetime in its center compared to its

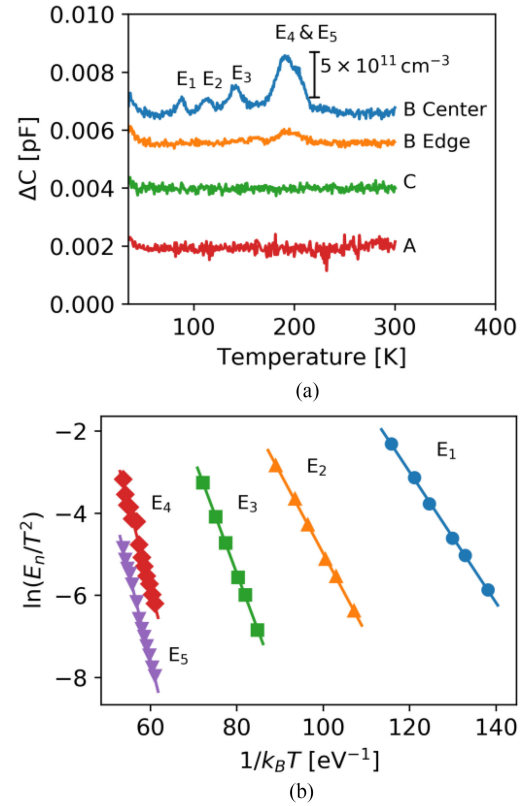


Fig. 3. (a) DLTS spectra measured on a representative sample from each group.  $\Delta C$  is the change of capacitance in the DLTS measurements. For sample from Group B, DLTS spectra measured from two different locations on the wafer are shown. The spectra are intentionally shifted in the vertical direction for clarity. The spectra were recorded with a reverse bias voltage  $U_b$  of  $-9$  V, a filling pulse voltage  $U_p$  of  $-4$  V, filling pulse length  $t_p$  of 1 ms, and an emission rate of  $50$  s $^{-1}$ . (b) Arrhenius plot of the five identified electron emission signals from the center of a sample in Group B.  $E_n$  is the electron emission rate,  $k_B$  is the Boltzmann constant, and  $T$  is absolute temperature.

periphery. The wafers from Group A (not annealed) and Group C (annealed at 1000 °C), on the contrary, both show uniformly high carrier lifetime. Regarding the injection-dependent lifetime, wafers from Groups A and C show similar lifetime curves with lifetime above 1 ms across the measured injection range. The lifetime measured at the center of the wafers from Group B is around 10  $\mu$ s, two orders of magnitude lower than that of wafers from Groups A and C.

These results agree with the findings in previous studies [16], [18], [21], [23]. Annealing at 500 °C activates bulk recombination-active defects in FZ silicon, whereas annealing at 1000 °C does not. Furthermore, the activated defects have a much higher impact in the center area of the wafer than at the periphery.

#### B. DLTS and MCTS: Energy Levels of the Activated Defects

The measured DLTS spectra of one typical sample from each group are shown in Fig. 3(a). As can be seen, four clear peaks appear in the DLTS spectrum recorded from the center of the degraded wafer (Group B). The relatively strong peak with its maximum at around 180 K also occurs in the spectrum measured



TABLE I  
EXTRACTED VALUE OF  $E_{na}$  AND  $\sigma_{na}$  FOR THE  $E_1$  TO  $E_5$  ELECTRON TRAPS  
IDENTIFIED IN THE CENTER OF A GROUP B SAMPLE

	$E_{na}$ [eV]	$\sigma_{na}$ [cm <sup>2</sup> ]
$E_1$	$0.16 \pm 0.005$	$1.15 \times 10^{-15}$
$E_2$	$0.20 \pm 0.005$	$3.7 \times 10^{-16}$
$E_3$	$0.28 \pm 0.005$	$4.2 \times 10^{-15}$
$E_4$	$0.41 \pm 0.01$	$1.5 \times 10^{-14}$
$E_5$	$0.43 \pm 0.01$	$1.2 \times 10^{-14}$

near the edge of this degraded wafer, however, with much smaller amplitude. A scale bar for the estimation of defect density  $N_t$  is also given in the figure. None of the peaks are observable in the DLTS spectra measured on wafers of Groups A and C. For clarity, the DLTS spectra measured on the samples from the edge area of the wafers from Groups A and C are not shown in Fig. 3(a). A Laplace-DLTS analysis [35], [36] indicates that the broad peak at around 180 K results from two electron emission signals, *i.e.*, it is a convolution of two peaks. Therefore, in total, there are five electron emission signals detected in samples from the center of the degraded wafers, labeled as  $E_1$  to  $E_5$ . Combining with the PL imaging results, it is likely that these five emission signals are related the thermally activated defects in FZ silicon.

Electron emission rates for the five detected traps were measured as a function of temperature. The activation energies  $E_{na}$  and apparent electron capture cross sections  $\sigma_{na}$  have been extracted from the Arrhenius plots shown in Fig. 3(b) and are listed in Table I. The detected defect levels are similar to the ones identified by Grant *et al.* [16], yet they differ from the ones recognized by Mullins *et al.* [23]. The detected  $E_1$ ,  $E_2$ , and  $E_3$  are similar to the ones detected by Hiller *et al.* [19], yet the detected  $E_4$  and  $E_5$  are different. One possible reason for these differences is that the activated defects in FZ silicon from different manufacturers might be different, due to the difference in the silicon growth condition. The FZ wafers used in this article are from the same manufacture as the ones used by Grant *et al.* [16] and have nitrogen present in the growth ambient to suppress the formation of extended defects. In the DLTS spectra measured by Grant *et al.* [16], the  $E_3$  emission signal has the highest peak height, whereas in our measurement, the  $E_4$  and  $E_5$  emission signals have the highest amplitude.

The electron capture characteristic of the five detected defect levels were also measured by varying the filling pulse length  $t_p$ . The actual  $\sigma_n$  of the  $E_5$  trap has been found to be temperature dependent according to  $\sigma_n = \sigma_\infty \exp(-E_\infty/k_bT)$  with a pre-exponential factor  $\sigma_\infty = 6.9 \times 10^{-16}$  cm<sup>2</sup> and an energy barrier  $E_\infty = 0.19$  eV. Unfortunately, since the changes in peak heights for  $E_1$  to  $E_4$  traps have been too small within the available range of  $t_p$  in our DLTS setup (1  $\mu$ s to 1 ms), we have not been able to extract their  $\sigma_n$  accurately.

Since DLTS on Schottky diodes only detects defect levels located in the majority carrier bandgap half (the upper half for *n*-type silicon), MCTS measurements were also performed in order to identify defect levels in the minority carrier bandgap half [37]. The measured MCTS spectra for one typical sample from each group are shown in Fig. 4(a). As can be seen, a peak related to hole emission is detected in the MCTS spectrum of

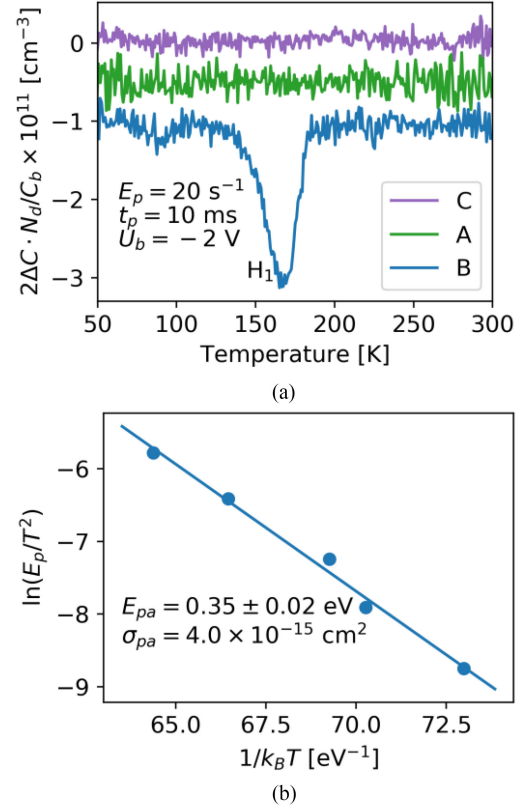


Fig. 4. (a) MCTS spectra for samples from the center of a representative wafer from each group.  $N_d$  is the doping concentration,  $C_b$  is the reverse bias capacitance,  $E_p$  is the hole emission rate. (b) Arrhenius plot of the identified hole emission signal.

the degraded sample (Group B), whereas no clear hole emission signal has been detected in the spectra of samples from Groups A and C. Therefore, this hole emission signal (labeled as  $H_1$ ) can also be correlated with the thermally activated defects.

The activation energy  $E_{pa}$  and apparent hole capture cross section  $\sigma_{pa}$  of the  $H_1$  trap were also extracted by measuring the hole emission rates at various temperature. The associated Arrhenius plot is shown in Fig. 4(b).  $E_{pa}$  is found to be  $0.35 \pm 0.02$  eV, while  $\sigma_{pa}$  is found to be  $4.0 \times 10^{-15}$  cm<sup>2</sup>. Unfortunately, due to the relatively low defect concentration, the actual hole capture cross section  $\sigma_p$  could not be accurately determined from direct capture measurements.

Based on the above DLTS and MCTS results alone, it is not possible to determine which level among the detected  $E_1$  to  $E_5$  electron traps and the  $H_1$  hole trap is the most detrimental one, or which level/levels should be responsible for the dramatic lifetime reduction of the degraded wafers.

### C. TIDLs: Characterization of the Dominant Defect Level

As lifetime spectroscopy allows defect parameters to be extracted directly from the measured lifetime, it is very sensitive to the dominant lifetime-degrading defect level(s) in the sample. Therefore, in this article, we use TIDLs to identify the dominant recombination-active defect levels of the thermally activated defects in FZ silicon.

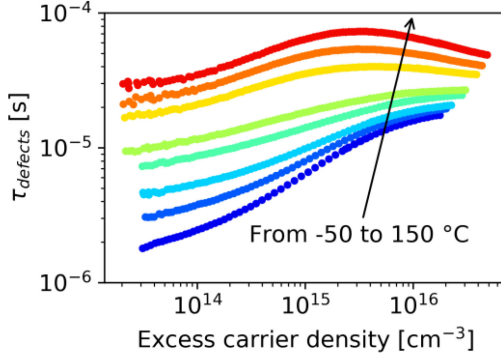


Fig. 5. Extracted lifetime calculated from (1) due to defects formed by 30 min annealing at 500 °C for all the lifetime measurement temperatures (−50 °C, −25 °C, 0 °C, 30 °C, 50 °C, 100 °C, 125 °C, and 150 °C).

It is first important to demonstrate that the temperature-dependent measurements themselves do not change the properties of the sample under investigation. The room temperature lifetime curves of the degraded wafer before and after TIDLS measurements are shown in Fig. 2. As can be seen, the temperature-dependent measurements do not change the lifetime significantly, indicating the heating during the TIDLS measurements does not change the concentration or properties of the dominant defects. Furthermore, the lifetime curve of the degraded wafer with a-Si passivation is almost identical to the one with superacid-derived passivation, indicating that 1) the effective lifetime of the sample is dominated by the activated bulk defects with these two different surface passivation techniques; and 2) the deposition of a-Si has not resulted in a change of the properties of the dominant defects.

For TIDLS analysis, we need to extract the defect associated recombination lifetime from the measured effective lifetime. As all wafers have the same intrinsic lifetime (due to Auger and band-to-band radiative recombination) by virtue of having the same doping, and, assuming that the surface recombination is constant, the following equation can be used to calculate the defects associated recombination lifetime:

$$\frac{1}{\tau_{\text{defects}}} = \frac{1}{\tau_B} - \frac{1}{\tau_C} \quad (1)$$

where  $\tau_B$  and  $\tau_C$  are the effective lifetime measured from the center of wafers from Group B (annealed at 500 °C) and wafers from Group C (annealed at 1000 °C), respectively. At all the measurement temperatures,  $\tau_B$  is always nearly two orders of magnitude lower than  $\tau_C$ , thus  $\tau_{\text{defects}}$  is very close to the measured  $\tau_B$ . This indicates that  $\tau_B$  is dominated by the recombination lifetime of the thermally activated defects. This also relaxes the previous assumption regarding identical intrinsic lifetime and SRV as they have little impact on the accuracy of the extracted  $\tau_{\text{defects}}$ . The extracted defect lifetime curve at all the measured temperatures is shown in Fig. 5. As can be seen,  $\tau_{\text{defects}}$  increases with the measurement temperature.

To gain insight into the recombination physics from lifetime measurements, we have replotted  $\tau_{\text{defects}}$  against a new variable  $Y \equiv p/n$ , where  $n$  and  $p$  are the concentration of free electrons

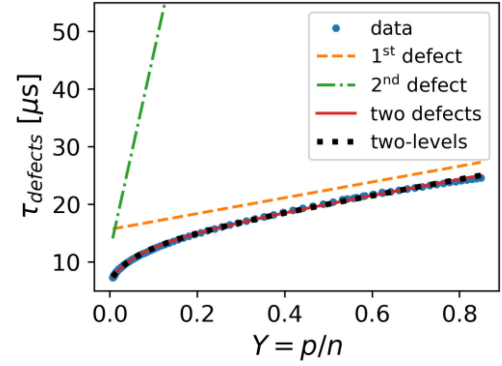


Fig. 6.  $\tau_{\text{defects}} - Y$  plot at 30 °C. The fitting of the data with two single-level defects or one two-level defect are overlaid.

and free holes, respectively. According to Murphy *et al.* [30], recombination lifetime resulting from a single-level defect which obeys Shockley–Read–Hall recombination statistics [38], [39] is a linear function of  $Y$  in  $n$ -type material. If the  $\tau_{\text{defects}} - Y$  plot is not linear, it indicates that  $\tau_{\text{defects}}$  is impacted by more than one defect level. The  $\tau_{\text{defects}} - Y$  plot at 30 °C is shown in Fig. 6. It is found that the  $\tau_{\text{defects}} - Y$  plots at all the measurement temperatures are concave curves and not straight lines.

This concave shape of  $\tau_{\text{defects}} - Y$  plots can be explained by the existence of two or more single-level defects or a multiple-level defect, or a mixture of them. We have tried to fit the experimentally derived data with two possible scenarios: 1)  $\tau_{\text{defects}}$  is dominated by two single-level defects; 2)  $\tau_{\text{defects}}$  is dominated by a two-level defect following the Sah–Shockley recombination statistics [40]. The fitting curves of these two scenarios are also shown in Fig. 6. As can be seen, both fitting approaches provide a good fit quality. In the following extraction of the dominant defect parameters, both possibilities are considered.

#### D. Defect Parameterization

In this section, we combine the information from DLTS/MCTS and TIDLS to extract the electrical properties ( $\sigma_n$  and  $\sigma_p$  and energy level  $E_t$ ) of the dominant recombination active defect levels among the thermally activated defects in FZ silicon. From DLTS/MCTS measurements, a judgment of the relative recombination activity of the detected defect levels is not certain. Moreover, because of significant changes in entropy resulting from charge state changes for some defects, the extracted apparent capture cross section can differ significantly from the actual capture cross section [41], [42]. The activation energy for carrier emission can also be different from the actual defect energy level [41], [42]. From IDLS at a single temperature, the defect parameterization is ambiguous, *i.e.*, it has an infinite number of solutions [31]. TIDLS can reduce this ambiguity, yet, it also suffers from the difficulty of temperature dependency of capture cross sections [28]. By combining the information from DLTS/MCTS and TIDLS, we expect to achieve a more accurate assessment of the electrical properties of the dominant defect level.

1) *Two Single-Level Defects:* We first consider the possibility that  $\tau_{\text{defects}}$  is dominated by two single-level defects. For

TABLE II  
TEMPERATURE DEPENDENCY OF CAPTURE CROSS SECTIONS

Label	Equation	Capture mechanism
Constant	$\sigma(T) = \text{constant}$	Classical Auger capture [44], or radiative capture [45]
Exponential law	$\sigma(T) = \sigma_\infty \exp\left(\frac{-E_\infty}{k_B T}\right)$	Multi-phonon emission capture [46]
Power law	$\sigma(T) = \sigma_0 T^{-\alpha}$	Cascade capture [47], or excitonic-enhanced Auger capture [48], [49]
Mix	$\sigma(T) = T^{-2} \exp\left(\frac{\Delta E}{k_B T}\right)$	Two-stage cascade capture [50]

TIDLS analysis, we use a modified defect parameter solution surface (DPSS) method [43] to extract the solution space of defect parameters at each temperature [28]. For each temperature, we obtained all the combinations of  $E_t$ ,  $N_t\sigma_n$ , and  $N_t\sigma_p$  that can provide the best fit of the measured lifetime. These combinations can be illustrated by the so-called DPSS curves. From Fig. 6, it appears that one of the single-level defects dominates most of the injection levels, whereas, the other defect only impacts the lifetime at very low injection conditions. The uncertainty in the extracted parameters for the less dominant defect can be significant, as a small uncertainty in the measured lifetime can propagate to a much larger uncertainty during the fitting. Therefore, in this article, we only focus on the defect parameters of the more dominant defect.

As mentioned above, from TIDLS, we extracted the full solution space of  $E_t$ ,  $N_t\sigma_n$ , and  $N_t\sigma_p$  at each temperature. Therefore, for each assumed value of  $E_t$ , the value of  $N_t\sigma_n$  and  $N_t\sigma_p$  at each temperature can be obtained. Since  $N_t$  is temperature independent, the temperature dependencies of  $\sigma_n$  and  $\sigma_p$  can be extracted. Four possible temperature dependencies of capture cross sections, which have been identified in the literature, are summarized in Table II. Therefore, for each assumed  $E_t$ , we can fit the extracted  $N_t\sigma_n(T)$  and  $N_t\sigma_p(T)$  with the four possible models. If at a certain value of  $E_t$ , both  $N_t\sigma_n(T)$  and  $N_t\sigma_p(T)$  can be well fitted with one of these four models, this  $E_t$  can be assumed as a possible solution.

The fitting quality of  $N_t\sigma_n(T)$  and  $N_t\sigma_p(T)$  is shown in Fig. 7. Here, we use the minimal fitting residual as the metric of the fitting quality. In this article, the fitting residual is defined

as  $\sqrt{\sum \left( \frac{F(x) - M(x)}{M(x)} \right)^2 / N_M}$ , where  $F$  is the function of the fitting,  $x$  is the independent variable of the function (herein the temperature),  $M$  is the measured data (herein the extracted  $N_t\sigma_n(T)$  or  $N_t\sigma_p(T)$ ), and  $N_M$  is the number of measured data. The  $M(x)$  in the denominator avoids increased fitting weight for the larger data points. The different symbols in Fig. 7 indicate which of the four possible models provides the best fitting quality at a certain assumed  $E_t$ . It can be noted that the symbols only exist in a certain range of  $E_t$  within the bandgap; this is because only in this range, the solution of  $E_t$ ,  $N_t\sigma_n$ , and  $N_t\sigma_p$  exists for all the measured temperatures.  $E_t$  values outside of this range are thus, excluded from the TIDLS solution space. Another point

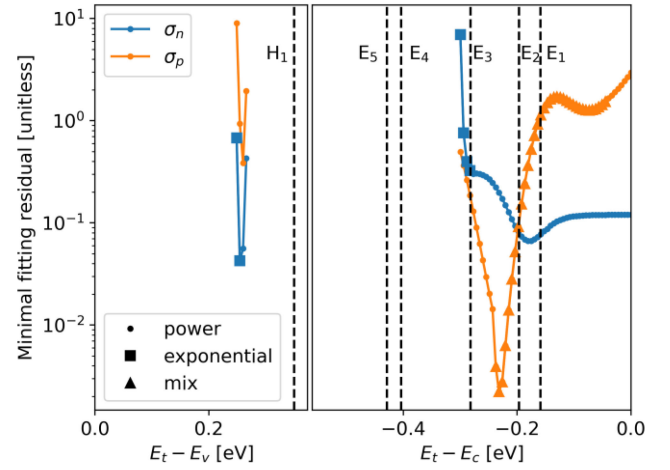


Fig. 7. Lowest residual values of fitting  $N_t\sigma_n(T)$  and  $N_t\sigma_p(T)$  of the dominant defect using the four possible temperature dependencies. The different symbols indicate the different temperature dependency that provides the optimal fitting. The vertical dashed lines indicate the activation energies of the emission signals detected by DLTS and MCTS.

to note is that the plots in Fig. 7 have only finite discrete data points. That is because the fitting here was done only to a finite number of  $E_t$ . Actually, within the solution range, there are infinite possible values for  $E_t$ . In Fig. 7, we also overlay the apparent defect levels identified by DLTS and MCTS as dashed lines.

From Fig. 7, we can first exclude the possibility of  $H_1$  as the dominant defect level. In the lower half of the bandgap, there is only a small range of  $E_t$  with solution. However, the activation energy extracted from MCTS for  $H_1$  is far away from this range (an energy difference of around 0.1 eV). This deviation cannot be explained by the temperature dependency of  $\sigma_p(T)$ . Within the solution range of  $E_t$  in the lower half of the bandgap, the optimal fitting for  $\sigma_p(T)$  is always the power law dependency and a power law temperature dependency of  $\sigma_p(T)$  will have only a small impact on the deviation of  $E_{pa}$  from the actual  $E_t$  (around 0.026 eV). This small impact cannot explain the large deviation of  $H_1$  activation energy to the possible solution range identified by TIDLS. With a similar reason, we can also exclude to possibility of the  $E_4$  being the dominant defect level.

The temperature dependency of  $\sigma_n(T)$  for  $E_5$  has been previously determined by DLTS and showed an exponential law temperature dependence. Taking this temperature dependency into consideration, the corrected  $E_t$  for  $E_5$  is obtained to be 0.24 eV below the conduction band edge  $E_C$ . However, as can be seen from Fig. 7, at this corrected  $E_t$ , the TIDLS results indicate that  $\sigma_n(T)$  should follow a power law. The fact that there is no solution around the value of  $E_5$  and the fact that the temperature dependence of the TIDLS fit contradicts the DLTS result excludes  $E_5$  as the dominant trap.

Therefore, only either  $E_1$ ,  $E_2$ , or  $E_3$  are likely to be the dominant defect level. However, the fitting quality of  $N_t\sigma_p(T)$  for  $E_1$  is much lower than that for the  $E_2$  and  $E_3$ , which makes it less likely to be the correct defect level. For  $E_2$  and  $E_3$ , the overall fitting quality of  $N_t\sigma_n(T)$  and  $N_t\sigma_p(T)$  is similar and we will now investigate these two levels in more details.

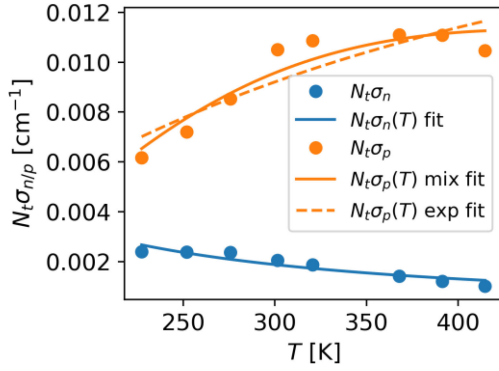


Fig. 8.  $N_t\sigma_n(T)$  and  $N_t\sigma_p(T)$  extracted at the activation energy of  $E_2$  for the dominant defect in TIDLS analysis. The blue line indicates the power law fit the  $N_t\sigma_n(T)$ . The orange solid line indicates the fit of  $N_t\sigma_p(T)$  with a mix of power law and exponential law. The orange dashed line indicates the fit of  $N_t\sigma_p(T)$  with the exponential law model.

TABLE III  
POSSIBLE PARAMETERS OF THE DOMINANT DEFECT ASSUMING TWO SINGLE-LEVEL DEFECTS

	$E_3$	$E_2$
$E_C - E_t$	$0.28 \pm 0.005$ eV	$0.21 \pm 0.01$ eV
$\sigma_n(T)$	$\sigma_n(T) = \text{constant}$	$\sigma_n(T) = \sigma_0 T^{-\alpha}$ $\alpha = 1.27$
$\sigma_p(T)$	$\sigma_p(T) = \sigma_0 T^{-\alpha}$ $\alpha = 1.86$	$\sigma_p(T) = T^{-2} \exp\left(\frac{\Delta E}{k_B T}\right)$ $\Delta E = -0.08$ eV $\sigma_p(T) = \sigma_\infty \exp\left(\frac{-E_\infty}{k_B T}\right)$ $E_\infty = 0.02$ eV
$k = \sigma_n/\sigma_p$ at 300 K	0.74	0.20

The  $N_t\sigma_n(T)$  and  $N_t\sigma_p(T)$  extracted from TIDLS at  $E_2$  is shown in Fig. 8. The optimal fitting of  $\sigma_n(T)$  is achieved by a power law model. The impact of this power law temperature dependency on the deviation of  $E_{na}$  from the actual  $E_t$  is estimated to be around 0.01 eV. The optimal fitting of  $\sigma_p(T)$  is achieved by a mix of exponential law and power law. However, fitting with an exponential law also provides a reasonably good fitting quality; thus, both temperature dependency models are possible. The fitting curves obtained from these two models are shown in Fig. 8 for comparison. The defect parameters extracted from fitting of the TIDLS curves upon the assumption of the  $E_2$  trap as the dominant recombination defect level are summarized in Table III.

We now investigate the possibility of the  $E_3$  trap as the dominant defect level. The extracted  $N_t\sigma_n(T)$  and  $N_t\sigma_p(T)$  from the TIDLS at  $E_3$  is shown in Fig. 9. At the activation energy of  $E_3$ , the optimal fitting for  $\sigma_n(T)$  is achieved by the exponential law model. However, it can be seen that  $\sigma_n$  does not increase monotonically with temperature, thus, a temperature independent  $\sigma_n$  seems to be more reasonable. The optimal fitting of  $\sigma_p(T)$  is achieved with the power law model. The defect parameters extracted from fitting of the TIDLS curves upon the assumption of the  $E_3$  trap as the dominant recombination defect level are also summarized in Table III.

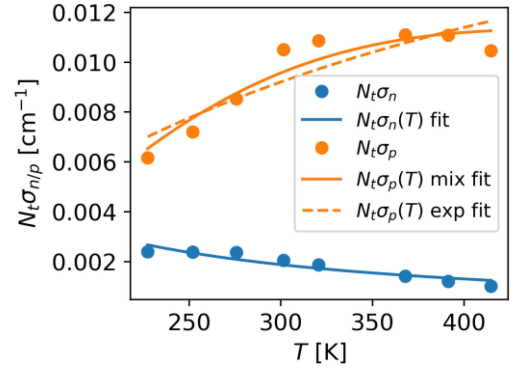


Fig. 9.  $N_t\sigma_n(T)$  and  $N_t\sigma_p(T)$  extracted at the activation energy of  $E_3$  for the dominant defect in TIDLS analysis. The blue line indicates the average value of  $N_t\sigma_n$ . The orange line indicates the fit of  $N_t\sigma_p(T)$  with the power law model.

Between  $E_2$  and  $E_3$ , the overall fitting quality of the temperature dependencies of the capture cross sections for  $E_2$  is slightly higher than for  $E_3$ . In this sense,  $E_2$  is more likely to be the dominant level. However, we can also calculate the extracted  $N_t\sigma_n$  and compare it with the values of  $N_t$  and  $\sigma_{na}$  products extracted from DLTS measurements. It is found that the  $E_3$  trap,  $N_t\sigma_n$  extracted from TIDLS is in the same order of magnitude as  $N_t\sigma_{na}$  extracted from DLTS, whereas for  $E_2$  these two values are one orders of magnitude different. With this consideration, it is more likely for the  $E_3$  trap to be the dominant defect. However, we are not able to completely rule out the possibility of  $E_2$  considering the uncertainty in the measurements.

2) *One Two-Level Defect*: Now we consider the case where the dominant defect is a two-level defect. As can be seen from Fig. 6, fitting under this assumption provides similar fitting quality to the case of two single-level defects. Therefore, it should not be ruled out as a possibility.

Here we use the method of two-levels defect parameterization proposed by Zhu *et al.* [51], [52]. Similar to the case of two single-level defects, the lifetime curve at each temperature is fitted independently. For each combination of two energy levels,  $E_{t1}$  and  $E_{t2}$ , the minimal fitting residual is illustrated in a two-dimensional map. The solution space of the defect parameters can be identified from the regions of the low fitting residuals. In Fig. 10, we present the sum of all the fitting residual maps. In this map, the regions of low residuals indicate the combinations of  $E_{t1}$  and  $E_{t2}$  that can provide good fitting quality to lifetime data at all measured temperatures.

In the regions of low fitting residuals in Fig. 10, we also fit the extracted  $N_t\sigma_{n1}(T)$ ,  $N_t\sigma_{p1}(T)$ ,  $N_t\sigma_{n2}(T)$ , and  $N_t\sigma_{p2}(T)$  with the four possible temperature dependencies of the capture cross section mentioned above. The subscript "1" and "2" here indicate the first level and the second level, respectively (not to confuse with the subscript number in  $E_1$  to  $E_5$  and  $H_1$ ). In this article, the first level refers to the transition energy between the most positively charged state and the middle charge state, whereas the second level refers to the transition energy between the middle state and the most negatively charged state.

The map of minimal fitting residual for fitting  $N_t\sigma_{n1}(T)$  with the four possible models is shown in Fig. 11. The corresponding



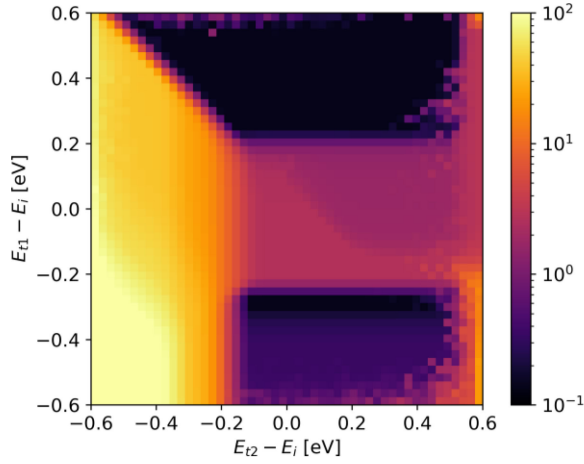


Fig. 10. Map of the sum of fitting residuals at each temperature with the assumption of a two-level defect. The two axes indicate the two energy levels of a two-level defect.

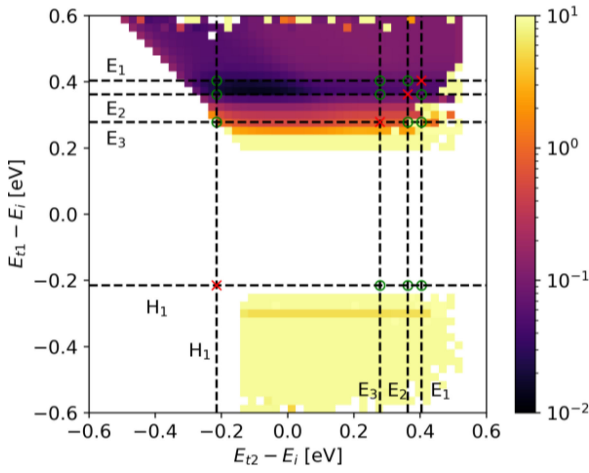


Fig. 11. Map of minimal fitting residual of fitting  $N_t \sigma_{n1}(T)$  with the four possible temperature dependencies. The dashed lines indicate the activation energies of  $E_1$ ,  $E_2$ ,  $E_3$ , and  $H_1$  identified by DLTS/MCTS.

maps for  $N_t \sigma_{n1}(T)$ ,  $N_t \sigma_{p1}(T)$ ,  $N_t \sigma_{n2}(T)$ , and  $N_t \sigma_{p2}(T)$  can be found in the support information. In Fig. 11, the activation energies of  $E_1$ ,  $E_2$ ,  $E_3$ , and  $H_1$  are indicated by horizontal and vertical dashed lines as they have similar estimated defect density from DLTS/MCTS measurements. The possible combination of  $(E_{t1}, E_{t2})$  should lie at the intersection of their corresponding lines (marked as green circles) except the ones from two identical levels (marked as red crosses).

From Fig. 11 and the other three maps for  $N_t \sigma_{p1}(T)$ ,  $N_t \sigma_{n2}(T)$ , and  $N_t \sigma_{p2}(T)$ , it is concluded that only for the combinations of  $(E_1, H_1)$  and  $(E_2, H_1)$  the fitting residuals for all four  $\sigma(T)$  are small. The extracted energy levels and  $\sigma(T)$  at these two possible combinations are summarized in Table IV. It should be noted that in both cases the  $\sigma_{n1}(T)$  and  $\sigma_{p2}(T)$  follows the power law temperature dependency, thus, it can be expected that the deviations between  $E_{na}$  and  $E_{t1}$  and between  $E_{pa}$  and  $E_{t2}$  are small.

TABLE IV  
POSSIBLE PARAMETERS OF THE DOMINANT DEFECT ASSUMING A TWO-LEVELS DEFECT

	Possibility 1	Possibility 2
$E_C - E_{t1}$	$0.16 \pm 0.01$ eV	$0.21 \pm 0.02$ eV
$\sigma_{n1}(T)$	$\sigma_0 T^{-\alpha}$ with $\alpha = 1.78$	$\sigma_0 T^{-\alpha}$ with $\alpha = 1.99$
$\sigma_{p1}(T)$	$T^{-2} \exp\left(\frac{\Delta E}{k_B T}\right)$ with $\Delta E = -0.11$ eV	$\sigma_\infty \exp\left(\frac{-E_\infty}{k_B T}\right)$ with $E_\infty = 0.03$ eV $T^{-2} \exp\left(\frac{\Delta E}{k_B T}\right)$ with $\Delta E = -0.09$ eV
$E_{t2} - E_V$	$0.35 \pm 0.02$ eV	$0.35 \pm 0.02$ eV
$\sigma_{n2}(T)$	$\sigma_\infty \exp\left(\frac{-E_\infty}{k_B T}\right)$ with $E_\infty = 0.13$ eV	$\sigma_\infty \exp\left(\frac{-E_\infty}{k_B T}\right)$ with $E_\infty = 0.12$ eV
$\sigma_{p2}(T)$	$\sigma_0 T^{-\alpha}$ with $\alpha = 5.41$	$\sigma_0 T^{-\alpha}$ with $\alpha = 5.16$
$k_1 = \sigma_{n1}/\sigma_{p1}$ at 300 K	0.035	0.193
$k_2 = \sigma_{n2}/\sigma_{p2}$ at 300 K	0.366	0.075
$\sigma_{n1}/\sigma_{n2}$ at 300 K	0.589	3.0

### E. Discussion

The above analysis of the dominant recombination defect levels considers the two cases: 1) two single-level defects, and 2) one two-level defect. Both cases provide satisfying fitting to the measured TIDLs data. However, we cannot completely exclude the possibility of more complicated cases, such as more than two single-level defects or a combination of single-level defects and multilevel defects. The two scenarios analyzed above are the simplest models which can provide good fitting of the measured lifetime data.

By combining the results of TIDLs with the results of DLTS/MCTS measurements on the same samples, we have extracted the possible electrical parameters of the dominant defect levels. However, the above analysis assumes that the dominant defect levels are among the ones detected by the DLTS/MCTS; this might not be true. For example, in the case of boron-oxygen-related defect responsible for light induced degradation of lifetime in Czochralski grown boron doped silicon wafers, the recombination defect level has not been reliably detected by DLTS, even though the defect has strong recombination activity as detected by lifetime measurements [53].

Finally, the above analysis also demonstrated the complexity of a full parameterization for a defect. Even though different techniques are used, we only identified several possible solutions of the defect parameters and are not able to make a decisive determination of the defect parameters. A sketch of the possible energy level positions of the identified dominant defect is shown in Fig. 12. One of the major difficulties originates from the temperature dependencies of the capture cross sections. Doping



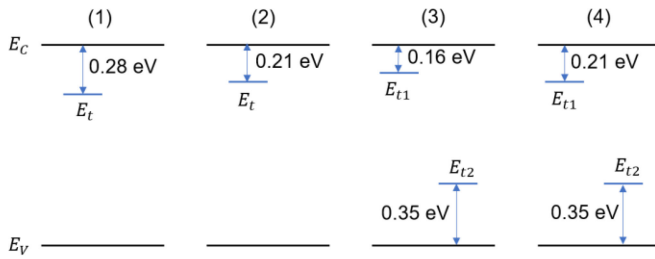


Fig. 12. Sketch of the energy level positions for the four possibilities of the dominant defect identified by a combined analysis of TIDLS and DLTS/MCTS.

dependent IDLS is an ideal technique to overcome this problem. However, it is essential to ensure that samples with various doping concentrations have the same defects. Previous studies indicate that these thermally activated defects could be different depending on the FZ silicon growth conditions [16], [18], [23]. Therefore, special care needs to be taken in the sample selection for doping dependent IDLS study.

#### IV. CONCLUSION

In this article, the thermally activated defects in *n*-type FZ silicon were investigated with a combination of TIDLS and DLTS/MCTS techniques. A thorough combined analysis of the data obtained by all the used techniques has been made to extract the electrical properties of the dominant recombination defect. From analysis of lifetime data, it was found that the most detrimental activated defects can be two single-level defects, or a defect with two energy levels. Both scenarios can provide satisfying fitting to the measured TIDLS data. The possible positions of energy levels and the temperature dependencies of capture cross sections for both scenarios were extracted. Measuring samples with various doping concentrations would be beneficial for a more decisive determination of the actual defect structure among these possibilities.

#### ACKNOWLEDGMENT

The supplemental information for this article is available at our website: <https://www.acdc-pv-unsw.com/journal2020>, or can be requested from the corresponding author. The views expressed herein are not necessarily the views of the Australian Government, and the Australian Government does not accept responsibility for any information or advice contained herein.

#### REFERENCES

- [1] W. Von Ammon, "FZ and CZ crystal growth: Cost driving factors and new perspectives," *Physica Status Solidi (a)*, vol. 211, no. 11, pp. 2461–2470, Sep. 2014.
- [2] J. Zhao, A. Wang, M. A. Green, and F. Ferrazza, "19.8% efficient 'honeycomb' textured multicrystalline and 24.4% monocrystalline silicon solar cells," *Appl. Phys. Lett.*, vol. 73, no. 14, pp. 1991–1993, Oct. 1998.
- [3] K. Yoshikawa *et al.*, "Silicon heterojunction solar cell with interdigitated back contacts for a photoconversion efficiency over 26%," *Nat. Energy*, vol. 2, no. 5, May 2017, Art. no. 17032.
- [4] C. Hollemann, F. Haase, S. Schäfer, J. Krügener, R. Brendel, and R. Peibst, "26.1%-efficient POLO-IBC cells: Quantification of electrical and optical loss mechanisms," *Prog. Photovolt.: Res. Appl.*, vol. 27, no. 11, pp. 950–958, Nov. 2019.
- [5] C. Sun, H. T. Nguyen, H. C. Sio, F. E. Rougieux, and D. Macdonald, "Activation kinetics of the boron–oxygen defect in compensated *n*- and *p*-type silicon studied by high-injection micro-photoluminescence," *IEEE J. Photovolt.*, vol. 7, no. 4, pp. 988–995, Jul. 2017.
- [6] M. A. Jensen *et al.*, "Evaluating root cause: The distinct roles of hydrogen and firing in activating light- and elevated temperature-induced degradation," *J. Appl. Phys.*, vol. 124, no. 8, Aug. 2018, Art. no. 085701.
- [7] K. Bothe and J. Schmidt, "Electronically activated boron-oxygen-related recombination centers in crystalline silicon," *J. Appl. Phys.*, vol. 99, no. 1, Jan. 2006, Art. no. 013701.
- [8] Z. Hameiri *et al.*, "Low-absorbing and thermally stable industrial silicon nitride films with very low surface recombination," *IEEE J. Photovolt.*, vol. 7, no. 4, pp. 996–1003, Jul. 2017.
- [9] W. Ji *et al.*, "Dip coating passivation of crystalline silicon by lewis acids," *ACS Nano*, vol. 13, no. 3, pp. 3723–3729, Mar. 2019.
- [10] A. I. Pointon, N. E. Grant, S. L. Pain, J. T. White, and J. D. Murphy, "Sub-2 cm/s passivation of silicon surfaces by aprotic solutions," *Appl. Phys. Lett.*, vol. 116, no. 12, Mar. 2020, Art. no. 121601.
- [11] A. Richter, S. W. Glunz, F. Werner, J. Schmidt, and A. Cuevas, "Improved quantitative description of Auger recombination in crystalline silicon," *Phys. Rev. B*, vol. 86, no. 16, 2012, Art. no. 165202.
- [12] D. Sperber, A. Herguth, and G. Hahn, "A 3-state defect model for light-induced degradation in boron-doped float-zone silicon," *Physica Status Solidi (RRL) - Rapid Res. Lett.*, vol. 11, no. 3, Mar. 2017, Art. no. 1600408.
- [13] T. Niewelt *et al.*, "Light-induced activation and deactivation of bulk defects in boron-doped float-zone silicon," *J. Appl. Phys.*, vol. 121, no. 18, May 2017, Art. no. 185702.
- [14] D. Bredemeier, D. Walter, S. Herlufsen, and J. Schmidt, "Understanding the light-induced lifetime degradation and regeneration in multicrystalline silicon," *Energy Procedia*, vol. 92, pp. 773–778, 2016.
- [15] D. Sperber, F. Furtwängler, A. Herguth, and G. Hahn, "Does LeTID occur in *c*-Si even without a firing step?," *AIP Conf. Proc.*, vol. 2147, 2019, Art. no. 140011.
- [16] N. E. Grant *et al.*, "Thermal activation and deactivation of grown-in defects limiting the lifetime of float-zone silicon," *Phys. Status Solidi (RRL) - Rapid Res. Lett.*, vol. 10, no. 6, pp. 443–447, Jun. 2016.
- [17] B. Hammann, J. Engelhardt, D. Sperber, A. Herguth, and G. Hahn, "Influencing light and elevated temperature induced degradation and surface-related degradation kinetics in float-zone silicon by varying the initial sample state," *IEEE J. Photovolt.*, vol. 10, no. 1, pp. 85–93, Jan. 2020.
- [18] N. E. Grant *et al.*, "Permanent annihilation of thermally activated defects which limit the lifetime of float-zone silicon," *Phys. Status Solidi (a)*, vol. 213, no. 11, pp. 2844–2849, 2016.
- [19] D. Hiller *et al.*, "Kinetics of bulk lifetime degradation in float-zone silicon: Fast activation and annihilation of grown-in defects and the role of hydrogen vs light," *Phys. Status Solidi (a)*, vol. 53, no. 9, 2020, Art. no. pssa.202000436.
- [20] B. Hoex *et al.*, "Ultralow surface recombination of *c*-Si substrates passivated by plasma-assisted atomic layer deposited  $\text{Al}_2\text{O}_3$ ," *Appl. Phys. Lett.*, vol. 89, no. 4, Jul. 2006, Art. no. 042112.
- [21] F. E. Rougieux, N. E. Grant, C. Barugkin, D. Macdonald, and J. D. Murphy, "Influence of annealing and bulk hydrogenation on lifetime-limiting defects in nitrogen-doped floating zone silicon," *IEEE J. Photovolt.*, vol. 5, no. 2, pp. 495–498, Mar. 2015.
- [22] Y. Zhu *et al.*, "New insights into the thermally activated defects in *n*-type float-zone silicon," in *Proc. AIP Conf. Proc.*, 2019, Art. no. 140014.
- [23] J. Mullins *et al.*, "Thermally activated defects in float zone silicon: Effect of nitrogen on the introduction of deep level states," *J. Appl. Phys.*, vol. 124, no. 3, Jul. 2018, Art. no. 035701.
- [24] T. Abe, "Generation and annihilation of point defects by doping impurities during FZ silicon crystal growth," *J. Crystal Growth*, vol. 334, no. 1, pp. 4–15, Nov. 2011.
- [25] T. Abe and T. Takahashi, "Intrinsic point defect behavior in silicon crystals during growth from the melt: A model derived from experimental results," *J. Crystal Growth*, vol. 334, no. 1, pp. 16–36, Nov. 2011.
- [26] V. V. Voronkov, "The mechanism of swirl defects formation in silicon," *J. Crystal Growth*, vol. 59, no. 3, pp. 625–643, Oct. 1982.
- [27] M. A. Khorosheva, V. I. Orlov, N. V. Abrosimov, and V. V. Kveder, "Determination of the nonequilibrium concentration of vacancies in silicon crystals by measuring the concentration of nickel atoms at lattice sites," *J. Exp. Theor. Phys.*, vol. 110, no. 5, pp. 769–774, May 2010.
- [28] S. Rein, *Lifetime Spectroscopy: A Method of Defect Characterization in Silicon for Photovoltaic Applications*, vol. 85. Berlin, Germany: Springer Science and Business Media, 2006.

- [29] J. Schmidt, "Temperature- and injection-dependent lifetime spectroscopy for the characterization of defect centers in semiconductors," *Appl. Phys. Lett.*, vol. 82, no. 13, pp. 2178–2180, Mar. 2003.
- [30] J. D. Murphy, K. Bothe, R. Krain, V. V. Voronkov, and R. J. Falster, "Parameterisation of injection-dependent lifetime measurements in semiconductors in terms of Shockley–Read–Hall statistics: An application to oxide precipitates in silicon," *J. Appl. Phys.*, vol. 111, no. 11, Jun. 2012, Art. no. 113709.
- [31] S. Rein, T. Rehrl, W. Warta, and S. W. Glunz, "Lifetime spectroscopy for defect characterization: Systematic analysis of the possibilities and restrictions," *J. Appl. Phys.*, vol. 91, no. 3, pp. 2059–2070, 2002.
- [32] N. E. Grant *et al.*, "Superacid-treated silicon surfaces: Extending the limit of carrier lifetime for photovoltaic applications," *IEEE J. Photovolt.*, vol. 7, no. 6, pp. 1574–1583, Nov. 2017.
- [33] A. I. Pointon, N. E. Grant, E. C. Wheeler-Jones, P. P. Altermatt, and J. D. Murphy, "Superacid-derived surface passivation for measurement of ultra-long lifetimes in silicon photovoltaic materials," *Sol. Energy Mater. Sol. Cells*, vol. 183, pp. 164–172, Aug. 2018.
- [34] C. Vargas *et al.*, "Recombination parameters of lifetime-limiting carrier-induced defects in multicrystalline silicon for solar cells," *Appl. Phys. Lett.*, vol. 110, no. 9, Feb. 2017, Art. no. 092106.
- [35] A. R. Peaker *et al.*, "Laplace deep level transient spectroscopy: Embodiment and evolution," *Phys. B: Condens. Matter*, vol. 407, no. 15, pp. 3026–3030, 2012.
- [36] L. Dobaczewski *et al.*, "Laplace-transform deep-level spectroscopy: The technique and its applications to the study of point defects in semiconductors," *J. Appl. Phys.*, vol. 96, no. 9, pp. 4689–4728, Nov. 2004.
- [37] R. Brunwin, B. Hamilton, P. Jordan, and A. R. Peaker, "Detection of minority-carrier traps using transient spectroscopy," *Electron. Lett.*, vol. 15, no. 12, pp. 349–350, 1979.
- [38] W. Shockley and W. T. Read, "Statistics of the recombination of holes and electrons," *Phys. Rev.*, vol. 87, no. 46, pp. 835–842, 1952.
- [39] R. N. Hall, "Electron-hole recombination in germanium," *Phys. Rev.*, vol. 87, no. 2, pp. 387–387, 1952.
- [40] C. Sah and W. Shockley, "Electron-hole recombination statistics in semiconductors through flaws with many charge conditions," *Phys. Rev.*, vol. 109, no. 4, pp. 1103–1115, 1958.
- [41] F. E. Rougieux, C. Sun, and D. Macdonald, "Determining the charge states and capture mechanisms of defects in silicon through accurate recombination analyses: A review," *Sol. Energy Mater. Sol. Cells*, vol. 187, pp. 263–272, Dec. 2018.
- [42] B. Peter and J. W. Orton, *The Electrical Characterization of Semiconductors: Majority Carriers and Electron States*. Cambridge, MA, USA: Academic Press, 1992.
- [43] A. E. Morishige *et al.*, "Lifetime spectroscopy investigation of light-induced degradation in p-type multicrystalline silicon PERC," *IEEE J. Photovolt.*, vol. 6, no. 6, pp. 1466–1472, Nov. 2016.
- [44] P. T. Landsberg, "Trap-Auger recombination in silicon of low carrier densities," *Appl. Phys. Lett.*, vol. 50, no. 12, pp. 745–747, Mar. 1987.
- [45] L. C. Kimerling, "Recombination enhanced defect reactions," *Solid State Electron.*, vol. 21, no. 11–12, pp. 1391–1401, 1978.
- [46] C. H. Henry and D. V. Lang, "Nonradiative capture and recombination by multiphonon emission in GaAs and GaP," *Phys. Rev. B*, vol. 15, no. 2, 1977, Art. no. 989.
- [47] A. Hangleiter, "Nonradiative recombination via deep impurity levels in silicon: Experiment," *Phys. Rev. B*, vol. 35, no. 17, 1987, Art. no. 9149.
- [48] A. Hangleiter and R. Häcker, "Enhancement of band-to-band auger recombination by electron-hole correlations," *Phys. Rev. Lett.*, vol. 65, no. 2, pp. 215–218, 1990.
- [49] P. T. Landsberg and D. J. Robbins, "The first 70 semiconductor auger processes," *Solid State Electron.*, vol. 21, no. 11–12, pp. 1289–1294, 1978.
- [50] R. M. Gibb *et al.*, "A two stage model for deep level capture," *Philos. Mag.*, vol. 36, no. 4, pp. 1021–1034, 1977.
- [51] Y. Zhu, G. Coletti, and Z. Hameiri, "Injection dependent lifetime spectroscopy for two-level defects in silicon," in *Proc. IEEE 46th Photovolt. Specialists Conf.*, Jun. 2019, pp. 0829–0832.
- [52] Y. Zhu, C. Sun, T. Niewelt, G. Coletti, and Z. Hameiri, "Investigation of two-level defects in injection dependent lifetime spectroscopy," *Sol. Energy Mater. Sol. Cells*, vol. 216, Oct. 2020, Art. no. 110692.
- [53] M. Vaquero-Contreras *et al.*, "Identification of the mechanism responsible for the boron oxygen light induced degradation in silicon photovoltaic cells," *J. Appl. Phys.*, vol. 125, no. 18, May 2019, Art. no. 185704.